

# T-Nb<sub>2</sub>O<sub>5</sub> (Orthorhombic)/C: An Efficient Electrode Material for Na-Ion Battery Application

Yenduri Bhaskara Rao, Naser Tavajohi, and Christian André Ohlin\*

Recently, niobium-based oxides have attracted attention as anode materials for sodium-ion battery (SIB) applications due to their rate and stability performance. However, reports on T-phase Nb<sub>2</sub>O<sub>5</sub> anode materials for SIB applications are rare. In this work, a simple and straightforward solid-state reaction to prepare a T-Nb<sub>2</sub>O<sub>5</sub> anode material using niobic acid, Nb<sub>2</sub>O<sub>5</sub>.nH<sub>2</sub>O, is proposed. Further, the active particles are successfully embedded in a carbon matrix derived from citric acid to enhance the electrochemical performance, with scanning electron microscopy demonstrating improved grain-to-grain contact following carbon coating. As a result, the coated sample (NC-1, mass ratio of 1:1

between niobic acid and citric acid) exhibits a high reversible capacity of 240 mA.h g<sup>-1</sup> at a current density of 25 mA g<sup>-1</sup>, compared to the uncoated sample (178 mA.h. g<sup>-1</sup>) due to increased surface area and porosity, better grain connectivity, and a more uniform carbon distribution. In addition, the carbon-coated sample displays a high rate capability of 180 mA.h g<sup>-1</sup> at 200 mA g<sup>-1</sup> and also delivers good cycling stability over 100 cycles with more than 99% Coulombic efficiency. The improved electrochemical performance is attributed to the presence of additional structural defects, enhanced particle contact, large pore volume, and high initial Coulombic efficiency.

## 1. Introduction

Sodium-ion batteries (SIBs) have attracted considerable attention recently as safer and cheaper substitutes for lithium-ion batteries (LIBs). As sodium resources are widely available, SIBs can be transported fully discharged, and sodium does not pose the same geopolitical risks as lithium.<sup>[1,2]</sup>

In addition, a battery system which is inexpensive, secure, and environmentally friendly is necessary for grid-scale energy storage—requirements that SIBs are better at meeting than LIBs. However, several issues restrict the widespread use of SIBs, such as slow Na<sup>+</sup>-ion diffusion kinetics, significant volume fluctuations, and structural pulverization during charging and discharging.<sup>[2]</sup> These challenges arise partly from the larger ionic radius of Na<sup>+</sup> compared to Li<sup>+</sup> (1.02 Å vs. 0.76 Å), which affects ion transport and structural compatibility with common electrode materials. As a result, many techniques and design strategies developed for high-performance LIBs require significant adaptation before they can be effectively applied to SIBs.<sup>[3]</sup> The current main scientific obstacle for a competitive SIB technology is developing viable anode materials, although recent research on

cathode materials for SIBs has yielded performances comparable to their lithium-ion counterparts.<sup>[4]</sup>

Graphite and other carbon-based materials have been employed as anode materials in commercial LIBs. However, the incorporation of the sodium ion into graphite layers is not thermodynamically favorable, which results in poor performance of SIBs.<sup>[5,6]</sup> Hard carbon is one of the promising anode materials that has good cycle performance and a large reversible capacity. However, the potential of Na/Na<sup>+</sup> is very close to the Na<sup>+</sup> insertion potential, which leads to Na metal deposition and dendrite formation that may raise safety issues for real-world applications. Conversely, the redox couple of Nb<sup>5+</sup>/Nb<sup>4+</sup> has the possibility to realize the reversible reaction with Na at an elevated potential as anode.<sup>[7]</sup> Thus, niobium-based oxide materials have been investigated as potential anodes for SIBs owing to their prominent pseudocapacitive behavior, high working potential, and high rate capability.<sup>[8]</sup> The five main polymorphs of niobium pentoxide, Nb<sub>2</sub>O<sub>5</sub>, are the pseudohexagonal (TT-Nb<sub>2</sub>O<sub>5</sub>), orthorhombic (T-Nb<sub>2</sub>O<sub>5</sub>), tetragonal (M-Nb<sub>2</sub>O<sub>5</sub>), monoclinic (H-Nb<sub>2</sub>O<sub>5</sub>), and amorphous structures (a-Nb<sub>2</sub>O<sub>5</sub>).<sup>[9]</sup> As calcination temperature increases, amorphous a-Nb<sub>2</sub>O<sub>5</sub>, TT-Nb<sub>2</sub>O<sub>5</sub>, T-Nb<sub>2</sub>O<sub>5</sub>, M-Nb<sub>2</sub>O<sub>5</sub>, and H-Nb<sub>2</sub>O<sub>5</sub> are gradually formed at different temperatures between 450 °C and 1100 °C.<sup>[8]</sup> Amorphous Nb<sub>2</sub>O<sub>5</sub> starts to crystallize at ≈600 °C to form TT-Nb<sub>2</sub>O<sub>5</sub> and proceeds to form orthorhombic T-Nb<sub>2</sub>O<sub>5</sub> at ≈800 °C. At higher temperatures, M-Nb<sub>2</sub>O<sub>5</sub> forms at ≈1000 °C, and when heated above 1000 °C monoclinic H-Nb<sub>2</sub>O<sub>5</sub> is obtained.<sup>[8]</sup> Out of these, the T-phase is the most promising one for SIB applications.

While the crystal structures of T-Nb<sub>2</sub>O<sub>5</sub> and TT-Nb<sub>2</sub>O<sub>5</sub> are similar, the disordered feature of TT-Nb<sub>2</sub>O<sub>5</sub> prevents the intercalation of Na<sup>+</sup>/Li<sup>+</sup> ions. Theoretical studies indicate that M-Nb<sub>2</sub>O<sub>5</sub> has a shorter Z-O (Z: alkali metal) distance than T-Nb<sub>2</sub>O<sub>5</sub> or TT-Nb<sub>2</sub>O<sub>5</sub>, suggesting a narrower diffusion channel that decreases ion mobility.<sup>[8]</sup> H-Nb<sub>2</sub>O<sub>5</sub> in turn exhibits battery-like properties in

Y. Bhaskara Rao, N. Tavajohi, C. André Ohlin  
Department of Chemistry  
Umeå University  
90187 Umeå, Sweden  
E-mail: andre.ohlin@umu.se

 Supporting information for this article is available on the WWW under <https://doi.org/10.1002/batt.202500134>

 © 2025 The Author(s). *Batteries & Supercaps* published by Wiley-VCH GmbH. This is an open access article under the terms of the Creative Commons Attribution-NonCommercial-NoDerivs License, which permits use and distribution in any medium, provided the original work is properly cited, the use is non-commercial and no modifications or adaptations are made.

which the material experiences a phase change upon (de)intercalation. As a result, the material may deliver high specific capacity but a modest rate performance.<sup>[10]</sup> In addition, the O array of H-Nb<sub>2</sub>O<sub>5</sub> is more densely packed and exhibits more repulsive intercalation than that of T-Nb<sub>2</sub>O<sub>5</sub>. In T-Nb<sub>2</sub>O<sub>5</sub>, the (001) lattice plane has a *d*-spacing of about 4 Å, which is larger than the diameter of Na<sup>+</sup>/Li<sup>+</sup> ions (2.04/1.52 Å), which promotes fast diffusion of mobile ions.<sup>[8]</sup> Na<sup>+</sup> ions are generally understood to undergo an intercalation-type mechanism in T-Nb<sub>2</sub>O<sub>5</sub> rather than alloying. Thus, T-Nb<sub>2</sub>O<sub>5</sub> exhibits a unique "intercalation pseudocapacitance" behavior within its crystal structure that enables rapid two-dimensional alkali ion transport without a phase transition during (de)intercalation.<sup>[10]</sup> This type of supercapacitor-like feature gives the material exceptional rate performance and a significant specific capacity.<sup>[11]</sup> The T-Nb<sub>2</sub>O<sub>5</sub> structure thus exhibits better electrochemical properties than the other forms. However, reports on T-Nb<sub>2</sub>O<sub>5</sub> as an anode material in SIB applications are few.

For instance, Yang et al. prepared ultrasmall T-Nb<sub>2</sub>O<sub>5</sub> nanocrystallites encapsulated in 1D carbon nanofibers using electro-spinning and reported a stable capacity of 150 mA.h.g<sup>-1</sup> at a current density of 1 A g<sup>-1</sup>.<sup>[12]</sup> In another study, T-Nb<sub>2</sub>O<sub>5</sub> nanocrystals uniformly coated on reduced graphene oxide sheets delivered a stabilized capacity of around 181 mA.h g<sup>-1</sup> at 0.2 A g<sup>-1</sup> after 100 cycles.<sup>[13]</sup> Other researchers found that self-supported, 3D porous, reticular Nb<sub>2</sub>O<sub>5</sub>@carbon thin films prepared by electrostatic spray deposition delivered a high reversible charge capacity of 271 mA.h g<sup>-1</sup> after 500 cycles at 0.5 C.<sup>[14]</sup>

Commercially available crystalline Nb<sub>2</sub>O<sub>5</sub> nanopowders consist mostly of H-phase (>1000 °C) and cannot be reverted to the other low-temperature (<1000 °C) phases, which is a major drawback. On the contrary, niobium precursors such as NbCl<sub>5</sub> and Nb(OC<sub>2</sub>H<sub>5</sub>)<sub>5</sub> are highly moisture-sensitive. Hydrous niobium oxide, or niobic acid (Nb<sub>2</sub>O<sub>5</sub>.nH<sub>2</sub>O), is amorphous and is used as a precursor in this work, which has an exceptionally high stability in addition to high activity and selectivity.<sup>[15,16]</sup> In addition, a simple and straightforward solid-state reaction is used, with a reaction temperature of 800 °C for 12 h.

While niobium oxide has high cycle durability and high rate capability resulting from the pseudocapacitive storage mechanism, the low ion diffusion and charge transfer limit battery performance.<sup>[13]</sup> This can be overcome by coating the niobium oxide with carbon-based materials, such as graphene and porous carbon. In this work, citric acid, an easily graphitizable carbon source,<sup>[17]</sup> is used as a chelating agent as well as a carbon source to coat the Nb<sub>2</sub>O<sub>5</sub> nanoparticles, with the aim of investigating the effect of carbon content on the electrochemical performance of the NC materials.

## 2. Results and Discussion

The XRD patterns of the niobic acid precursor and the annealed samples (NC) are shown in Figure 1a and illustrate the amorphous nature of hydrous niobium oxide precursor prior to annealing. After heating the precursor at 800 °C, crystalline peaks are observed in the NC-0 sample, which lacks carbon, without any secondary phase being present. All diffraction peaks of the sample are indexed to orthorhombic Nb<sub>2</sub>O<sub>5</sub> (T-Nb<sub>2</sub>O<sub>5</sub>, COD#210-6534) with a *Pbam* space group.<sup>[18,19]</sup> This structure is made up of Nb atoms encircled by oxygen atoms to form pentagonal bipyramids or deformed octahedra. Through corner-sharing, the NbO<sub>7</sub> and NbO<sub>6</sub> polyhedra are aligned along the *c*-axis to generate an alternative layered structure with a layer spacing of 3.9 Å.<sup>[20]</sup> Following carbon coating, the three samples (NC-0.5, NC-1, and NC-2) display the same orthorhombic phase, but with broad peaks indicating the smaller crystallite size compared to that of the base T-Nb<sub>2</sub>O<sub>5</sub> sample, NC-0. The Rietveld refinement of the XRD patterns of four materials was conducted using the Profex software, and the results are presented in Figure S1, Supporting Information. Further, the crystallite sizes of the four materials, determined by using the Scherrer formula, are provided in Table 1. It is observed that the crystallite size values of NC-0.5, NC-1, and NC-2 materials are reduced significantly after carbon coating compared to that of the uncoated sample, NC-0. Thus, the Na<sup>+</sup>-ion transport can be facilitated by the smaller crystallites

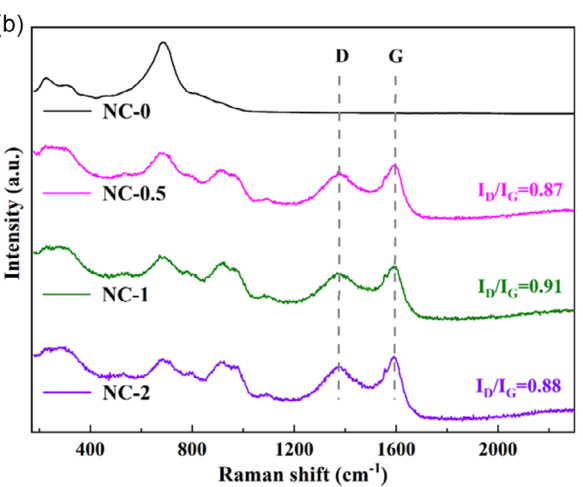
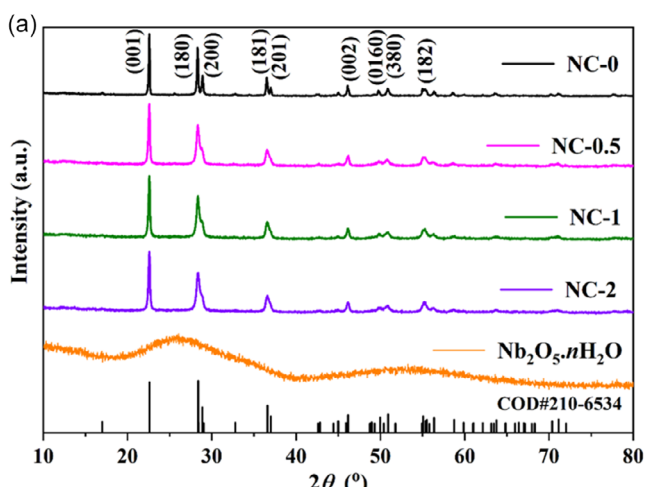


Figure 1. a) XRD patterns of Nb<sub>2</sub>O<sub>5</sub>.nH<sub>2</sub>O, NC-0, NC-0.5, NC-1, and NC-2 materials and b) Raman spectra of NC-0, NC-0.5, NC-1, and NC-2 materials.

**Table 1.** The crystallite size, degree of disorder, BET-specific surface area, pore volume, and reversible discharge capacity at 25 mA g<sup>-1</sup> and *b* value from power law relationship for all the four materials, NC-0, NC-0.5, NC-1, and NC-2.

Sample	Crystallite size [nm]	$I_D/I_G$	$S_{BET}$ [m <sup>2</sup> g <sup>-1</sup> ]	Pore volume [cm <sup>3</sup> g <sup>-1</sup> ]	Specific capacity [mA.h g <sup>-1</sup> ]	<i>b</i> from power law
NC-0	51.60	NA	2.22	0.000066	177.6	1.01
NC-0.5	32.12	0.87	29.50	0.001080	200.1	1.04
NC-1	32.69	0.91	41.52	0.001755	239.6	1.08
NC-2	30.99	0.88	50.31	0.001154	220.1	1.06

and improved grain-to-grain contact. Further, Raman spectra (Figure 1b) are used to analyze the vibrational energy modes of all the four samples along with the degree of graphitization in carbon-coated samples. The bands between 200 and 550 cm<sup>-1</sup> are attributed to the bending modes of NbO<sub>6</sub>, whereas the broadband close to 700 cm<sup>-1</sup> is associated with the stretching modes of NbO<sub>6</sub>.<sup>[21]</sup> Additionally, the bands between 600–700 cm<sup>-1</sup> are responsible for the Nb-O bending modes, and the bands near 980 cm<sup>-1</sup> are assigned to the Nb-O double bond stretch mode.<sup>[22]</sup> Further, the two distinctive peaks labeled D and G in Figure 1b originate from the graphite lattice, where the D-signal ( $\approx$ 1380 cm<sup>-1</sup>) denotes the lattice defects, and the G-band ( $\approx$ 1600 cm<sup>-1</sup>) denotes the stretching vibration mode of the graphite lattice. The degree of amorphous structure in NC-labeled samples can be ascertained by analyzing the intensity ratio ( $I_D/I_G$ ) of the D to G peaks, and the different materials, NC-0.5, NC-1, and NC-2 have ratios of 0.87, 0.91, and 0.88, respectively (Table 1). The three materials have  $I_D/I_G$  values fairly close to one, indicating that the ordered graphene sheets are highly defective and thus affect the electrochemical characteristics of the NC electrode.

SEM and TEM were used to analyze the morphology and microstructure of the NC-0 and NC-1 materials (Figure 2). Although micron-sized particles are present in both materials, the NC-1 sample shows a superior grain-to-grain connection following carbon coating. TEM images (Figure 2b,e) reveal the morphology of carbon-coated material, NC-1, and it is unaffected by the surface modification. The preferred crystal orientations of NC-0 (inset: Figure 2b) and NC-1 (inset: Figure 2e) materials are evident from the SAED pattern. Specifically, the NC-1 sample exhibits a hollow ring pattern along with bright spots, suggesting that the NC active particles are surrounded by an amorphous or disordered carbon framework.<sup>[23,24]</sup> HRTEM images further reveal the lattice fringes in both materials (Figure 2c,f), confirming their crystalline nature. Additionally, a thin amorphous layer around the NC active particles in the NC-1 material (Figure 2f) indicates that the niobium oxide material is successfully embedded and decorated with the carbon matrix. Finally, the EDX elemental mapping images confirm the uniform distribution of Nb and O in the base material, NC-0 (Figure 2h,i), and Nb, O, and C in the carbon-coated material, NC-1 (Figure 2k-m).

The valence states and surface characteristics of NC-0 and NC-1 samples were examined using XPS analysis. The presence of C is confirmed in the coated material, NC-1, presented in the XPS survey spectra (Figure 3a), along with Nb and O elements

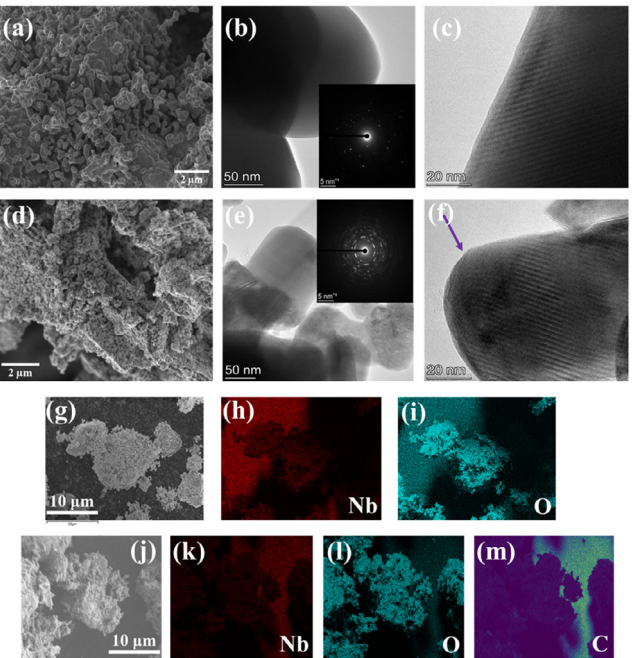


**Figure 2.** SEM, TEM, and HRTEM images of a-c) NC-0 and d-f) NC-1 materials (inset: SAED pattern), and electron diffraction X-ray spectroscopy (EDX) images of g-i) NC-0 and j-m) NC-1 materials.

(NC-0). A high-resolution C 1s XPS spectrum (Figure 3b), in NC-1 material, exhibited six prominent peaks at the binding energies of 284.4, 285.7, 286.8, 288.0, 289.7, and 292.3 eV, which are responsible for C-C, C-OH, C-O-C, O-C=O, COOH, and  $\pi$ - $\pi^*$  peaks, respectively.<sup>[25,26]</sup> A Nb 3d spectrum, displayed in Figure 3c,e, consists of two main peaks at 207.5 and 210.2 eV, which are assigned to Nb 3d<sub>5/2</sub> and Nb 3d<sub>3/2</sub>, respectively, and conforming the presence of Nb<sup>5+</sup> in both samples.<sup>[27]</sup> Additionally, in both samples, the O 1s peak (Figure 3d,f) deconvolutes into three peaks that are centered about 530.5, 531.5, and 532.5 eV, respectively, representing Nb-O, C-OH/C-O-C, and C=O bonds.<sup>[28]</sup>

Further, the specific surface area and pore size distribution of each of the four materials are ascertained by analyzing the N<sub>2</sub> adsorption-desorption isotherm (Figure 3). All of the carbon-coated samples in Figure 3g showed a hysteresis loop at high P/P<sub>0</sub> and an isotherm of type IV typical behavior, indicating the presence of large mesoporous structures upon carbon coating.<sup>[29]</sup> Varying the carbon content leads to differences in specific surface area and porosity; thus, the samples NC-0, NC-0.5, NC-1, and NC-2 have respective BET-specific surface areas ( $S_{BET}$ ) of 2.22, 29.50, 41.52, and 50.31 m<sup>2</sup> g<sup>-1</sup>. In addition, the relative pore volumes of 0.000066, 0.001080, 0.001755, and 0.001154 cm<sup>3</sup> g<sup>-1</sup> for the four materials, respectively, indicate that the coated materials have a large number of active sites compared to the base material. The observed variations in porosity arose inherently from the carbon-coating process, which depended on the amount of citric acid used. Specifically, the NC-1 sample exhibits a larger pore volume than that of other samples (Table 1). The BJH mean pore diameters (Figure 3h) of the four materials, NC-0, NC-0.5, NC-1, and NC-2, are found to be 55, 10, 9, and 8 nm, respectively. Therefore, the pore volume and surface area of the three coated

samples can be significantly increased by the addition of carbon coating to the NC active particles.

**Figure 4** displays the cyclic voltammogram curves for each prepared electrode at the three initial cycles, in the voltage range of 0.01–2.5 V. Two distinct cathodic and anodic peaks at 0.01 V are visible in the CV curves in each case, and they are ascribed to the sodium insertion and extraction into the NC material. The irreversible reduction peak  $\approx 0.4$  V in the first cycle is due to the electrolyte decomposition and/or formation of a solid electrolyte interphase (SEI) film.<sup>[30]</sup> Additionally, the broad reduction peak shifts to the higher potential side (0.5 V), suggesting that the

electrode shows decreased resistance.<sup>[7]</sup> The CV curves nearly overlap in the following cycles, indicating that the Na insertion and extraction are highly reversible.

Further, the electrochemical performance of all the four samples in the initial three charge–discharge cycles at a current density of  $25 \text{ mA g}^{-1}$  is shown in **Figure 5**. The uncoated sample, NC-0, delivered the initial discharge and charge specific capacities of  $224.8$ ,  $158.2 \text{ mA.h g}^{-1}$ , respectively, whereas the coated samples, NC-0.5, NC-1, and NC-2 delivered the enhanced discharge/charge capacities of  $272.1/175.7$ ,  $326.6/224.3$ , and  $321.9/207.7 \text{ mA.h g}^{-1}$  which corresponds to initial coulombic

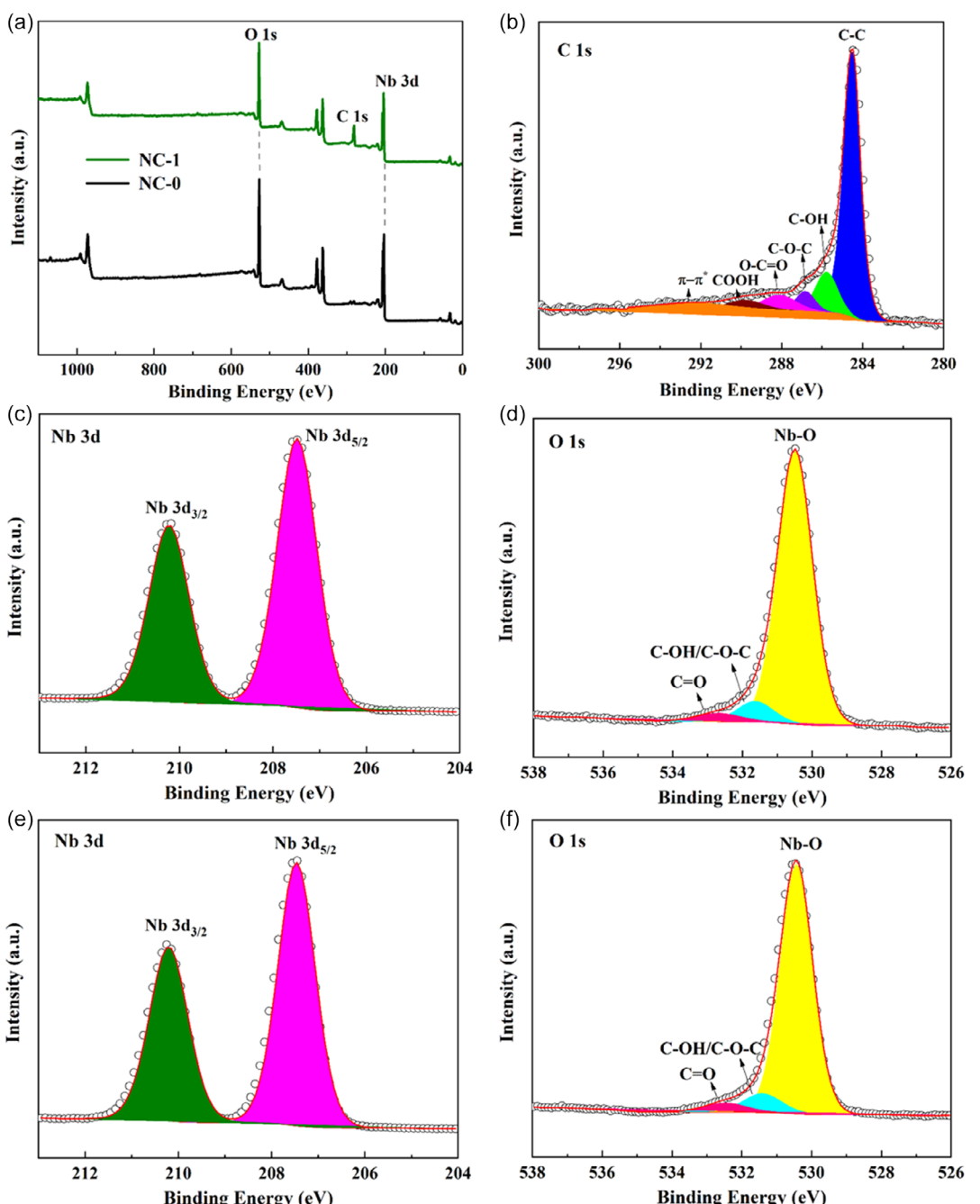


**Figure 3.** a) XPS survey spectra, b) C 1s, c) Nb 3d, d) O 1s of NC-1, and e) Nb 3d, f) O 1s of NC-0 materials, and g) N<sub>2</sub>-adsorption and desorption isotherms, and h) pore size distribution of NC-0, NC-0.5, NC-1, and NC-2 materials.

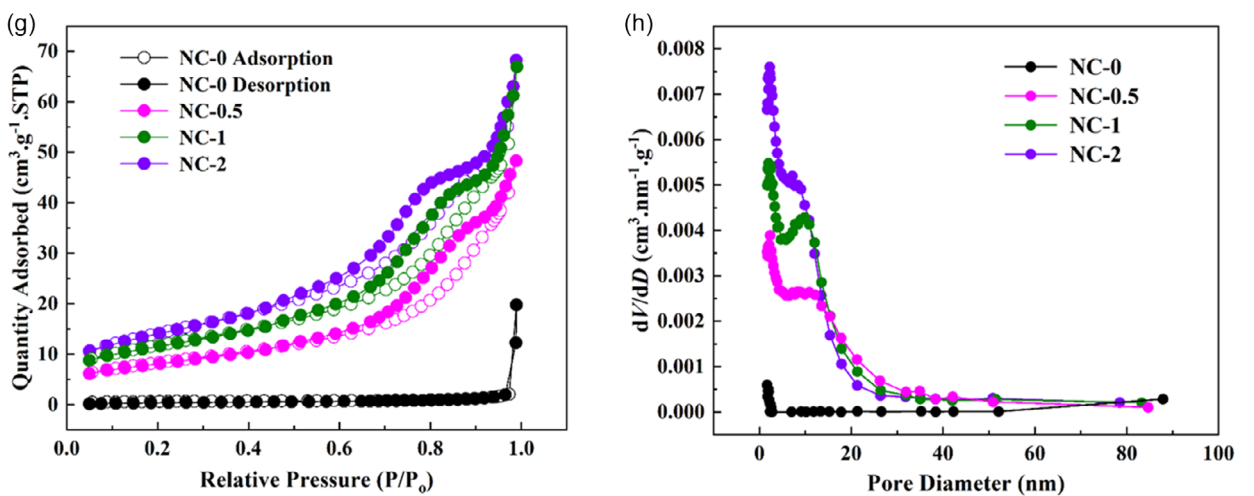


Figure 3. Continued.

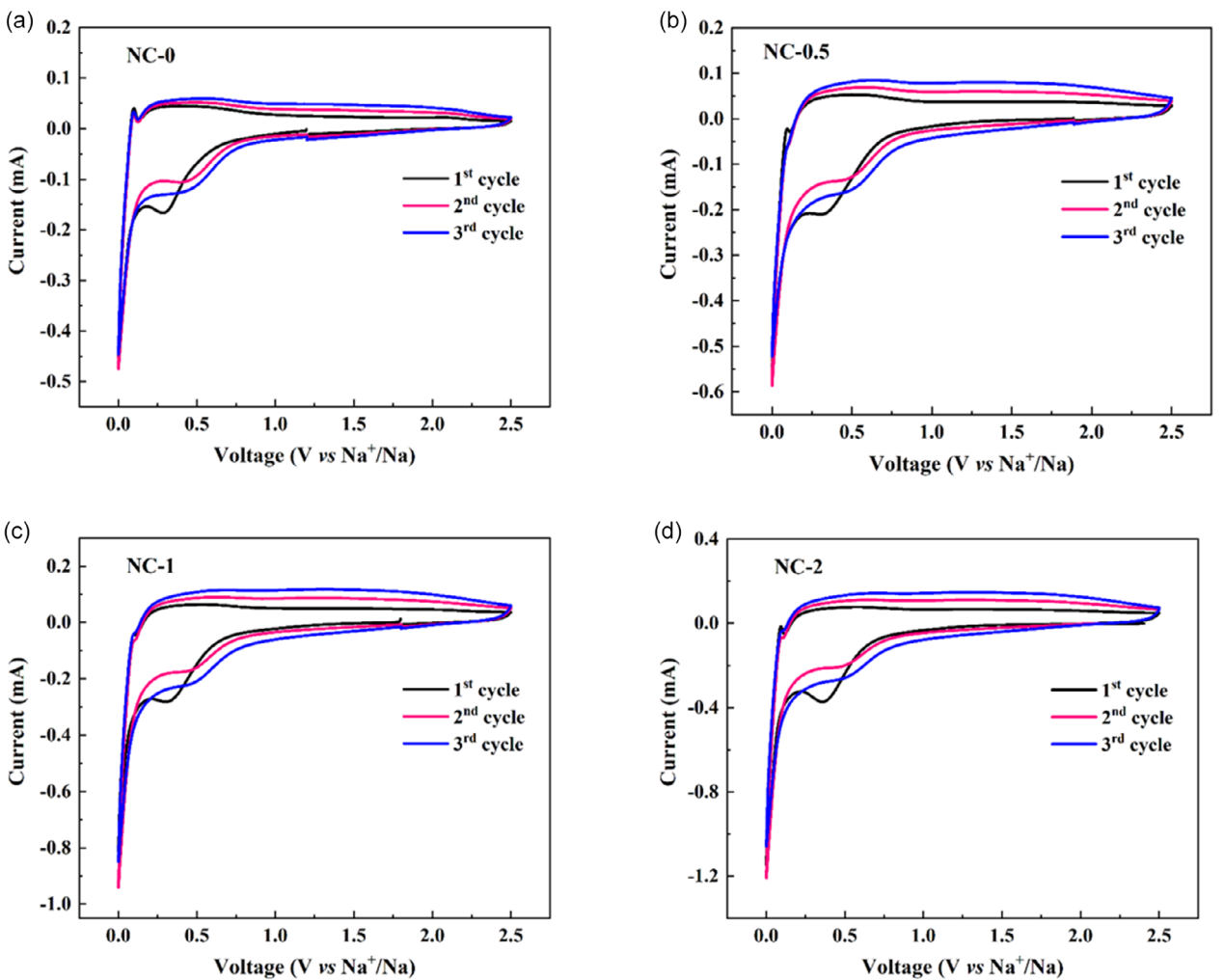
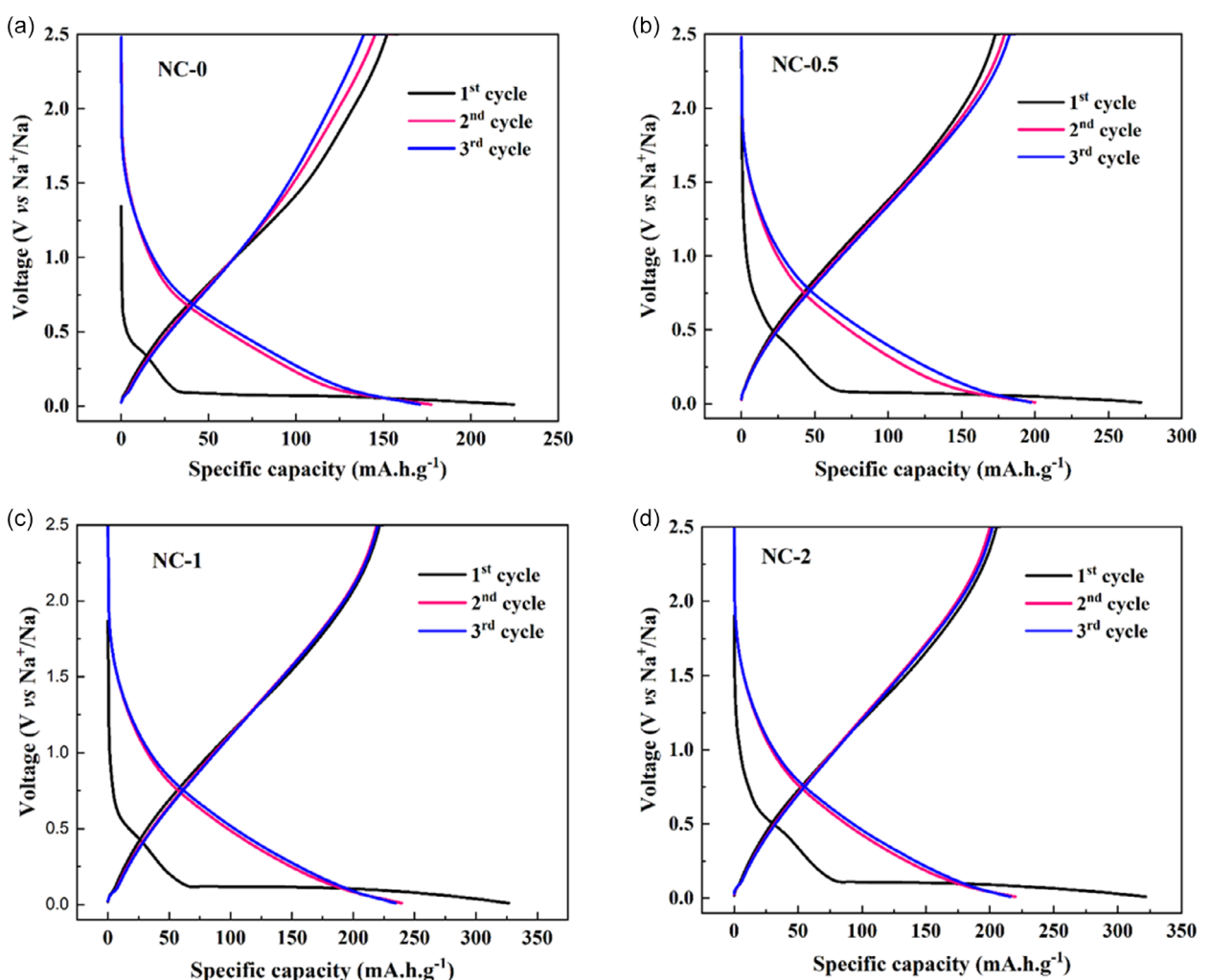


Figure 4. CV of a) NC-0, b) NC-0.5, c) NC-1, and d) NC-2 materials.

efficiencies of 65%, 69%, and 65%, respectively, in comparison to the base material (70%). The irreversible capacity loss in the first cycle is caused by the formation of an SEI layer or the degradation

of liquid electrolytes for all samples that are consistent with the CV results (Figure 4). In the case of coated samples, the loss is higher, which could be due to the ability of carbon to absorb



**Figure 5.** Galvanostatic charge–discharge curves of a) NC-0, b) NC-0.5, c) NC-1, and d) NC-2 materials for the first three cycles.

more liquid electrolytes, which raises the resistance at the SEI layer.<sup>[31]</sup> All four samples, however, show reversible and durable electrochemical kinetics by recording high reversible discharge capacities of 177.6, 200.1, 239.6, and 220.1 mA.h g<sup>-1</sup> for NC-0, NC-0.5, NC-1, and NC-2 samples, respectively (Table 1). Thus, from the second cycle, more than 92% coulombic efficiency is achieved in all the samples, indicating their good electrochemical stability.

An ex situ XRD measurement is performed using the coin-type cell as described in the experimental section to better understand the Na<sup>+</sup>-ion insertion/extraction behavior. The standard Cu peaks are seen at  $2\theta$  values of 43.37, 50.49, and 74.13 (Figure S2, Supporting Information). Further, the changes in the crystal structure of all the four electrodes are analyzed after three complete discharge cycles. It is clear from Figure S2a and b, Supporting Information, that there is no phase change occurring during the discharge process. In addition, the diffraction peak (001) shifts to a lower angle side (Figure S2c, Supporting Information), after discharging to 0.01 V, indicating the expansion of *d*-spacing upon Na<sup>+</sup>-ion intercalation in the NC-2 material.<sup>[32]</sup> Similar behavior is observed in the other three electrodes, and thus it is clear that all the four NC electrodes reversibly react with the sodium during the charge/discharge process.

**Figure 6a** shows the rate performance of each of the four NC samples at different current densities. The pristine sample, NC-0, displayed the discharge specific capacities of 178, 131, 91, 72, 46, 28, 10, and 1 mA.h g<sup>-1</sup> at current densities of 25, 50, 100, 200, 500, 1000, 2000, and 5000 mA.g<sup>-1</sup>, respectively. On the other side, the carbon-coated sample, NC-0.5 delivered the enhanced discharge capacities of 200, 176, 145, 113, 63, 30, 10, and 1 mA.h g<sup>-1</sup>, whereas, NC-2 delivered the discharge capacities of 220, 202, 182, 160, 128, 95, 54, and 17 mA.h g<sup>-1</sup>, respectively, at the same current densities. However, the carbon-coated sample, NC-1, delivered high discharge capacities of 240, 219, 201, 180, 147, 110, 64, and 23 mA.h g<sup>-1</sup>, respectively, at the same current densities among the other samples. Because of the ideal doping/coating of C surrounding the NC active particles, NC-1 demonstrated a better rate capability than the other samples at every current rate. Also, the NC-1 electrode offers additional redox active sites for the storage of Na<sup>+</sup> ions due to its more disordered nature (Figure 1b).<sup>[29]</sup> Furthermore, it is important to note that when the current rate is returned to the initial value (25 mA g<sup>-1</sup>), the uncoated sample, NC-0, only showed a discharge capacity of 84 mA.h g<sup>-1</sup>, which corresponds to only 47% capacity recovery. However, the carbon-coated samples, NC-0.5, NC-1, and NC-2,

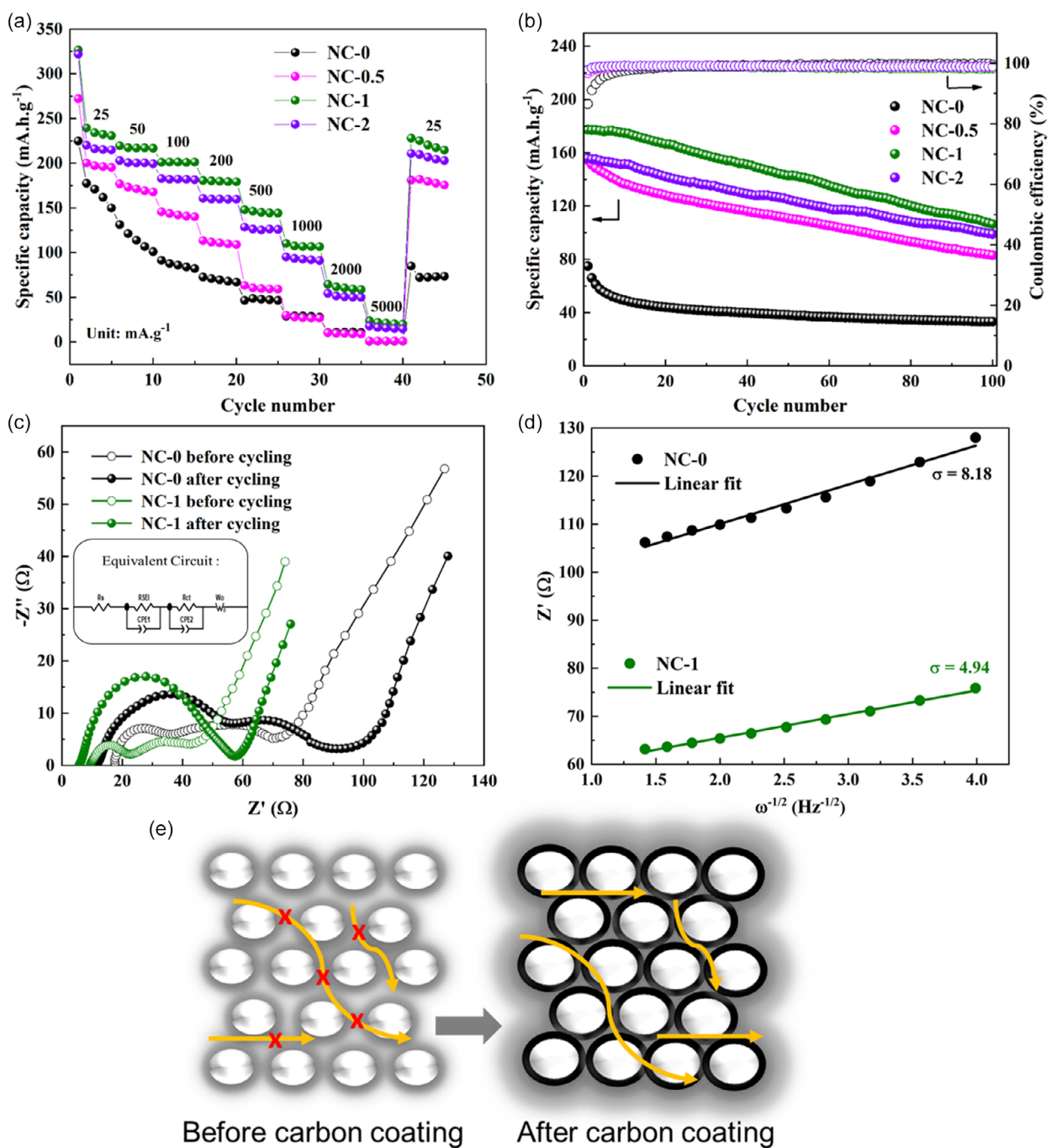


**Figure 6.** a) Rate performance at various current densities, b) cycling stability at a current density of 200 mA g<sup>-1</sup> of NC-0, NC-0.5, NC-1, and NC-2 materials, c) Nyquist plots, before and after cycling (inset: equivalent circuit), d) fitting curves of  $Z'$  and  $\omega^{-1/2}$  at a low-frequency region of NC-0 and NC-1 materials, and e) schematic showing the transport of ions.

delivered more than 95% specific capacity recovery, even after returning to the initial current rate, demonstrating their superior reversibility and remarkable stability. Additionally, Figure 6b illustrates the long-term cycling stability of all four materials at a current density of 200 mA g<sup>-1</sup> across the voltage range of 0.01 and 2.5 V. It is obvious from the figure that all the samples exhibit consistent coulombic efficiencies of  $\approx 99\%$  during the cycling. Nevertheless, the pristine sample, NC-0, delivers a discharge capacity of 33 mA.h g<sup>-1</sup> only after 100 cycles. Such a poor cycling

performance is observed and may be due to the formation of an inactive interface layer, resulting from the reaction between the electrode and organic electrolyte, which finally leads to an increase in its interfacial resistance during the cycling.<sup>[33]</sup> Conversely, superior reversible capacities of 83, 106, and 98 mA.h g<sup>-1</sup> were recorded by the coated samples, NC-0.5, NC-1, and NC-2, respectively, after 100 cycles. Further, the electrochemical performance of the NC-0 and NC-1 electrodes is compared with some of the other oxide materials in the literature (Table 2).

Anode material	Preparation	Potential window [V vs Na <sup>+</sup> /Na]	Specific capacity [mA.h g <sup>-1</sup> ]	Current density [mA g <sup>-1</sup> ]	Reference
Na <sub>0.23</sub> TiO <sub>2</sub>	Molten salt route	0.05–2.5	150	50	[44]
Ta <sub>2</sub> O <sub>5</sub>	Sol-gel	0.01–3.0	123	100	[45]
TiNb <sub>2</sub> O <sub>7</sub>	Ball milling	0.01–2.5	180	15	[46]
TiO <sub>2</sub>	Hydrothermal	0.8–3.0	77	50	[47]
KNb <sub>3</sub> O <sub>8</sub> @F-C	Solution-assisted solid-state reaction	0.01–2.5	173	10	[48]
Nb <sub>2</sub> O <sub>5</sub> (NC-0)	Solid-state reaction	0.01–2.5	178	25	This work
Nb <sub>2</sub> O <sub>5</sub> @C (NC-1)	Solid-state reaction	0.01–2.5	240	25	This work

The enhanced rate and cycling performances are further analyzed with the help of EIS for the base sample, NC-0, and the best-performing coated sample, NC-1, before and after 20 cycles of discharge and charge (Figure 6c). The equivalent circuit, shown in the inset of Figure 6c, is used to fit the Nyquist plots, which consist of the solution resistance  $R_s$ , SEI layer resistance  $R_{SEI}$ , and the charge transfer resistance  $R_{ct}$ .<sup>[34]</sup> In the case of the NC-0 electrode, higher charge transfer resistances of 40 and 48 Ω are recorded before and after cycling, respectively, may be due to the poor contact among NC active particles (Figure 6e). On the contrary, significantly smaller charge transfer resistances of 21 and 23 Ω are recorded for the carbon-coated sample, NC-1, before and after cycling, respectively. Because of the improved grain-to-grain contact (Figure 6e), the carbon-coated sample may thus accomplish a stronger interfacial charge transfer capability, which is advantageous for its high, stable rate performance and decent cycling stability in the electrode material.

Furthermore, the charge transfer resistance and the improved electrochemical rate performance are directly related to the Na<sup>+</sup>-ion diffusion coefficient,  $D_{Na^+}$ , and it can be computed by Equation (1).<sup>[35]</sup>

$$D_{Na^+} = \frac{R^2 T^2}{2A^2 n^4 F^4 C_{Na^+}^2 \sigma^2} \quad (1)$$

where  $R$  is the gas constant,  $T$  is the temperature,  $F$  is the Faraday constant,  $n$ ,  $A$ ,  $\sigma$ , and  $C$  represent the number of transferred electrons, the effective working area of the electrode, the slope of  $Z'$  versus  $\omega^{-1/2}$  and the Na<sup>+</sup>-ion concentration, respectively. Using Equation (2)<sup>[36]</sup>

$$Z' = R_s + R_{SEI} + R_{ct} + \sigma\omega^{-1/2} \quad (2)$$

the slope ( $\sigma$ ) can be determined by using the plot between  $Z'$  and  $\omega^{-1/2}$  (Figure 6d). After substituting all the values, the NC-1 electrode records a significantly higher sodium-ion diffusion coefficient of  $1.08 \times 10^{-10} \text{ cm}^2 \text{ s}^{-1}$ , while the base sample, NC-0 achieved only  $3.93 \times 10^{-11} \text{ cm}^2 \text{ s}^{-1}$ . Thus, the fast movement of Na<sup>+</sup>-ions, resulting from the improved grain-to-grain contact (illustrated in Figure 6e) in the carbon-coated material, enhances the electrochemical performance of the NC-1 material.<sup>[37]</sup>

Figure 7a,b displays the CV plots of the NC-0 and NC-1 materials at different scan rates. For both materials, the anodic and cathodic peak currents increase as the scan rate increases, and

the better symmetry of the redox peaks indicates that the electrodes exhibit better reversibility. Additionally, a slight increase in the oxidation potential indicates that the polarization in both electrode materials is smaller.<sup>[38]</sup> To further investigate the electrode kinetics in both materials, the power law relationship is used (Equation (3)).<sup>[39]</sup>

$$i_p = av^b \quad (3)$$

where  $i_p$  is the peak current,  $v$  is the scan rate, and  $a$  and  $b$  are constants obtained from fitting. Equation (3) can be rewritten as Equation (4).

$$\log(i_p) = \log(a) + b \log(v) \quad (4)$$

Here, the slope  $b$  can be obtained from a linear fit of the graph between  $\log(v)$  and  $\log(i_p)$  (Figure 7c), and the value can be used to depict the capacitive and diffusion-controlled contributions.<sup>[40]</sup> From Figure 7c, the  $b$  values of all the four materials, NC-0, NC-0.5, NC-1, and NC-2, are found to be 1.01, 1.04, 1.08, and 1.06, respectively (Table 1), which indicates that the Na<sup>+</sup>-ion storage mechanisms are controlled mostly by the capacitive processes. Furthermore, Equation (5) yields the quantitative repartition of the diffusive and capacitive contributions to the overall storage mechanism of the materials.<sup>[41,42]</sup>

$$i(V) = k_1 v + k_2 v^{1/2} \quad (5)$$

where  $k_1 v$  and  $k_2 v^{1/2}$  denote the surface capacitive and the diffusion-controlled contributions, respectively. The capacitive and diffusive contributions on the CV plots of NC-0 and NC-1 electrodes at a scan rate of  $0.2 \text{ mV.s}^{-1}$  are shown in Figure 7d,e. It is clear from Figure 7f that the percentage of capacitive contribution increases gradually as the scan rate increases from  $0.2$  to  $1 \text{ mV.s}^{-1}$ . This is because, under higher rate conditions, surface capacitance dominates the total capacity. Concurrently, the diffusion-regulated capacity contribution decreases as the slow intercalation speed is unable to satisfy the needs of the high rate of electrochemical processes at higher scan rates.<sup>[43]</sup> Thus, the NC-1 electrode exhibits remarkable electrochemical performance due to the carbon-coating layer surrounding the NC active particles over the other electrode materials, which makes it a promising anode material for the development of high-performance SIBs.

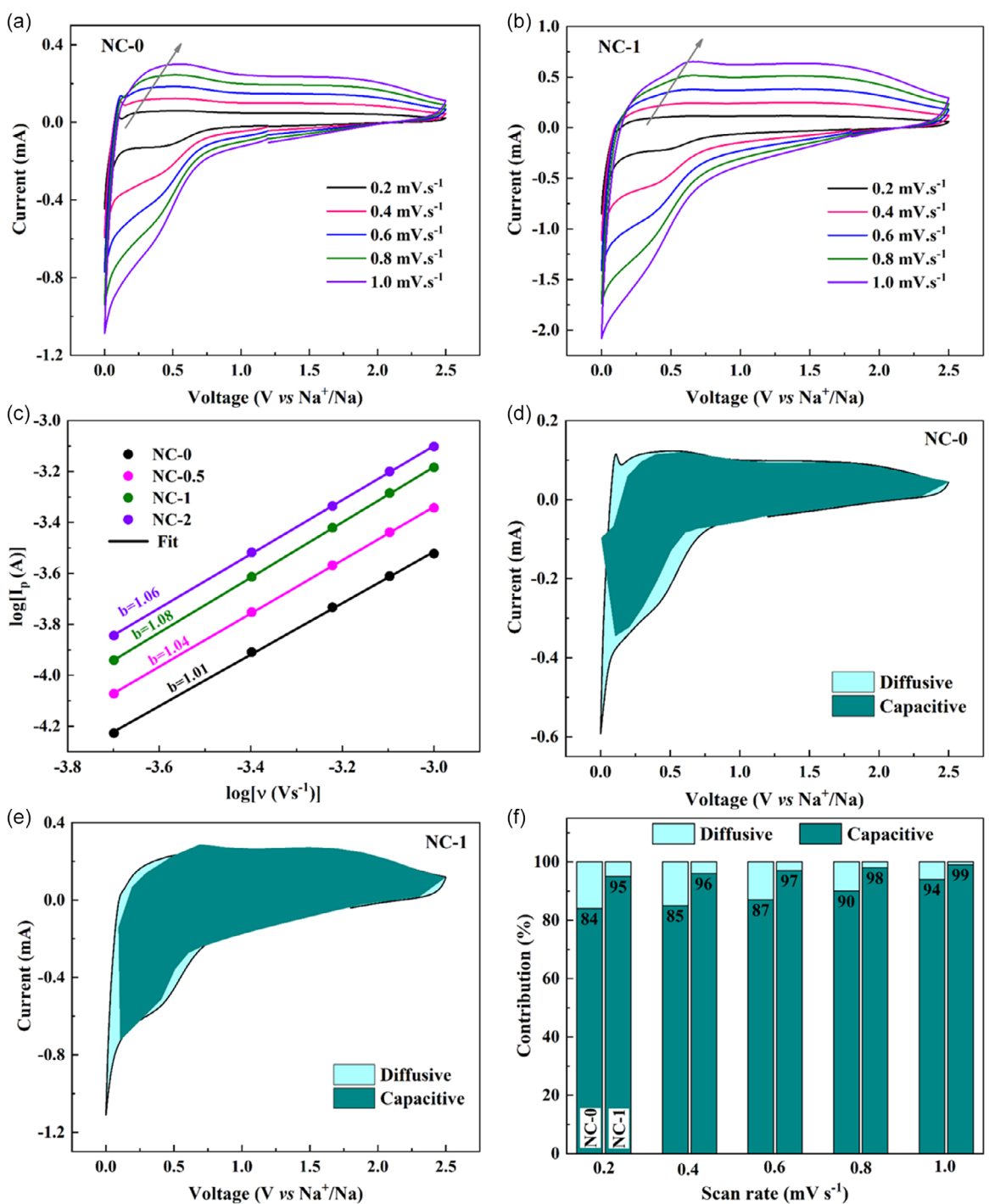


**Figure 7.** Cyclic voltammogram at various scan rates for a) NC-0 and b) NC-1 materials; c) plot of logarithm of scan rate versus logarithm of peak current of NC-0, NC-0.5, NC-1, and NC-2 materials, CV curve showing the diffusive and capacitive contribution of d) NC-0 and e) NC-1 materials at 0.2 mV s<sup>-1</sup> scan rate; f) percentage contribution of diffusive and capacitive processes at various scan rates for NC-0 and NC-1 materials.

### 3. Conclusion

T-Nb<sub>2</sub>O<sub>5</sub> electrode material was prepared by a facile one-step solid-state reaction using niobic acid as a precursor rather than complex and lengthy synthesis procedures. Further, the active particles were successfully embedded with carbon matrix to enhance the electrochemical performance. As a result, the carbon-coated samples achieved improved structural defects,

better grain-to-grain electrical contact, large specific surface area, and large pore volume. In particular, the NC-1 material (optimal ratio, 1:1) exhibited a high reversible capacity of 240 mA.h g<sup>-1</sup> at 25 mA g<sup>-1</sup> and enhanced rate performance of 180 mA.h g<sup>-1</sup> at 200 mA g<sup>-1</sup> due to its large pore volume, high Na<sup>+</sup>-ion diffusion coefficient, and inherent pseudocapacitive behavior. Finally, the coated materials exhibited good cycling stability compared to the uncoated material over 100 cycles. Thus, the present study

enables the T-Nb<sub>2</sub>O<sub>5</sub>/C electrode as a promising anode material for the development of SIB technology using an easy, affordable, and scalable method.

## 4. Experimental Section

### Material Synthesis

Niobic acid (Nb<sub>2</sub>O<sub>5</sub>·nH<sub>2</sub>O; 40% H<sub>2</sub>O w/w), obtained as a gift from Prof. William H. Casey (UC Davis), was heated directly in an electric furnace (Nabertherm, Germany) at 800 °C for 12 h to obtain the crystalline T-Nb<sub>2</sub>O<sub>5</sub> powder. For carbon-coated samples, the desired amount of citric acid (C<sub>6</sub>H<sub>8</sub>O<sub>7</sub>, Sigma-Aldrich) and niobic acid were mixed in an agate mortar and pestle with ethanol as a mixing medium. The product was then air dried and calcined at 800 °C for 2 h under an N<sub>2</sub> atmosphere to obtain the final samples. The four samples were named NC-0 (1:0), NC-0.5 (1:0.5), NC-1 (1:1), and NC-2 (1:2), according to the weight ratio between niobic acid and anhydrous citric acid.

### Material Characterization

The crystal structure of the materials was examined by X-ray diffraction (XRD) spectroscopy conducted on a PANalytical Xpert3 powder X-ray diffractometer employing Cu-K $\alpha$  radiation. The samples were scanned in the 2 $\theta$  range of 10–80° at a step size of 0.02626. The Raman spectra were recorded using a Renishaw Qontor instrument (Renishaw Plc, UK) running WiRe (version 5.3). In normal confocality mode, a 532 nm solid-state laser with a nominal maximum power of 50 mW was employed through a 20x lens. A Zeiss Merlin Schottkey field emission gun (FEG)-scanning electron microscopy (SEM) equipped with a GEMINI II column was used to gather SEM images. The corresponding image showed the working distance, the probe current, and the acceleration voltage (or electron high tension, EHT). A Ceta-D 4 k  $\times$  4 k complementary metal oxide semiconductor (CMOS) detector was used to capture high-resolution transmission electron microscopy (HRTEM) images on the Field Electron and Ion company (FEI) Glacios 200 kV cryo-TEM. The TEM grids were made of lacey carbon film coated with (400 squares per inch) copper TEM grid mesh. A 40  $\mu$ m or 100  $\mu$ m aperture was employed for selected area electron diffraction (SAED) images to filter out anything other than the particle of interest. The X-ray photoelectron spectroscopy (XPS) was obtained using a Kratos Axis Ultra delay-line detector (DLD) electron spectrometer equipped with a monochromated Al K $\alpha$  source running at 150 W. Wide spectra were obtained using an analyzer pass energy of 160 eV, while individual photoelectron lines were detected at 20 eV. Kratos software was used for spectral processing. A Micromeritics TriStar 3000 porosimeter was used to perform N<sub>2</sub> adsorption–desorption tests. Following 3 h of outgassing the samples at 120 °C, the isotherms were observed at –196 °C. The Brunauer–Emmett–Teller (BET) method was used to gather the specific surface areas, and the desorption isotherms were used to compute the pore volumes. Using the ASAP-2010 program, the Barret, Joyner, and Halenda (BJH) algorithm was used to estimate the pore size distributions.

### Electrochemical Characterization

CR-2032 coin-type half-cells built in an argon-filled glove box (MBraun-MB10-compact) with O<sub>2</sub> and H<sub>2</sub>O levels < 0.5 ppm were used for the electrochemical testing. The active substance (80 wt%), Super P (Thermo Scientific) (15 wt%), and sodium carboxymethylcellulose (CMC-MedChemExpress; 5 wt%) binder were mixed with deionized water to prepare each electrode. A copper foil (TMAXCN; 14 mm diameter, 0.1 mm thick) current collector was covered with the mixture and allowed to dry at 50 °C. The electrode

loading was 2–3 mg cm<sup>-2</sup>. The electrolyte was 1 M NaClO<sub>4</sub> (Thermo Scientific) in ethylene carbonate (from AmBeed) and dimethyl carbonate (DMC, from TCI; 1:1 v/v), and the separator was a glass microfiber filter (Whatman, Grade GF/F; 19 mm diameter). Sodium metal was used as the counter/reference electrode in the fabrication of coin cells. A Gamry 1010E interface workstation was used to record electrochemical impedance spectroscopy (EIS) in the frequency range of 10 mHz to 1 MHz and cyclic voltammetry (CV) curves at various scan rates. The galvanostatic charge–discharge curves were recorded using a NEWARE CT-4008 battery tester within a voltage window of 0.01–2.5 V (vs. Na<sup>+</sup>/Na). Every electrochemical measurement was carried out at 20 °C.

For ex situ XRD characterization, the CR-2032 coin-type cells were disassembled inside the Ar-filled glove box with O<sub>2</sub> and H<sub>2</sub>O levels < 0.5 ppm after three complete discharge cycles. The recovered electrodes were then washed with DMC to remove any residual liquid electrolyte and dried in the glove box overnight.

### Acknowledgements

The authors thank the Kempe foundation (JCSMK22-0094) for financial support and acknowledge the facilities and technical assistance of the Umeå Centre for Electron Microscopy (UCEM) at the Chemical Biological Centre (KBC), Umeå University, Sweden.

### Conflict of Interest

The authors declare no conflict of interest.

### Data Availability Statement

The data that support the findings of this study are available from the corresponding author upon reasonable request.

**Keywords:** anode materials · carbon coatings · electrochemistry · niobic acids · sodium-ion batteries · solid-state reactions · t-nb<sub>2</sub>O<sub>5</sub>

- [1] S. W. Kim, D. H. Seo, X. Ma, G. Ceder, K. Kang, *Adv. Energy Mater.* **2012**, 2, 710.
- [2] S. Liu, J. Feng, X. Bian, J. Liu, H. Xu, *Energy Environ. Sci.* **2016**, 9, 1229.
- [3] M. Dahbi, N. Yabuuchi, K. Kubota, K. Tokiwa, S. Komaba, *Phys. Chem. Chem. Phys.* **2014**, 16, 15007.
- [4] M. He, S. Liu, J. Wu, J. Zhu, *Prog. Solid State Chem.* **2024**, 74, 100452.
- [5] F. Xie, Z. Xu, Z. Guo, M. M. Titirici, *Prog. Energy* **2020**, 2, 042002.
- [6] H. Kim, J. Hong, G. Yoon, H. Kim, K. Y. Park, M. S. Park, W. S. Yoon, K. Kang, *Energy Environ. Sci.* **2015**, 8, 2963.
- [7] H. Nakayama, M. Nose, S. Nakanishi, H. Iba, *J. Power Sources* **2015**, 287, 158.
- [8] T. F. Yi, H. M. K. Sari, X. Li, F. Wang, Y. R. Zhu, J. Hu, J. Zhang, X. Li, *Nano Energy* **2021**, 85, 105955.
- [9] H. Ding, Z. Song, H. Zhang, X. Li, *Mater. Today Nano* **2020**, 11, 100082.
- [10] J. Lin, S. Zhao, T. G. Tranter, Z. Zhang, F. Peng, D. Brett, R. Jervis, P. R. Shearing, *Electrochim. Acta* **2023**, 443, 141983.
- [11] L. Kong, C. Zhang, J. Wang, W. Qiao, L. Ling, D. Long, *Sci. Rep.* **2016**, 6, 21177.
- [12] L. Yang, Y. E. Zhu, J. Sheng, F. Li, B. Tang, Y. Zhang, Z. Zhou, *Small* **2017**, 13, 1702588.
- [13] L. Yan, G. Chen, S. Sarker, S. Richins, H. Wang, W. Xu, X. Rui, H. Luo, *ACS Appl. Mater. Interfaces* **2016**, 8, 22213.
- [14] H. Yang, R. Xu, Y. Gong, Y. Yao, L. Gu, Y. Yu, *Nano Energy* **2018**, 48, 448.
- [15] K. Tanabe, *Mater. Chem. Phys.* **1987**, 17, 217.

- [16] M. A. Rambaran, A. Gorzsas, M. Holmboe, C. A. Ohlin, *Dalt. Trans.* **2021**, *50*, 16030.
- [17] J. Wang, J. Bi, W. Wang, Z. Xing, Y. Bai, M. Leng, X. Gao, *J. Electrochem. Soc.* **2020**, *167*, 090539.
- [18] S. Li, Q. Xu, E. Uchaker, X. Cao, G. Cao, *CrystEngComm* **2016**, *18*, 2532.
- [19] L. Kong, C. Zhang, S. Zhang, J. Wang, R. Cai, C. Lv, W. Qiao, L. Ling, D. Long, *J. Mater. Chem. A* **2014**, *2*, 17962.
- [20] P. Shen, B. Zhang, Y. Wang, X. Liu, C. Yu, T. Xu, S. S. Mofarah, Y. Yu, Y. Liu, H. Sun, H. Arandiyan, *J. Nanostructure Chem.* **2021**, *11*, 33.
- [21] M. R. Joya, J. J. Barba Ortega, A. M. Raba Paez, J. G. da Silva Filho, P. D. T. Cavalcante Freire, *Metals Basel.* **2017**, *7*, 142.
- [22] C. Cao, D. Ford, S. Bishnoi, T. Proslier, B. Albee, E. Hommerding, A. Korczakowski, L. Cooley, G. Ciavati, J. F. Zasadzinski, *Phys. Rev. Spec. Top. - Accel. Beams* **2013**, *16*, 064701.
- [23] Y. Da Cho, G. T. K. Fey, H. M. Kao, *J. Power Sources* **2009**, *189*, 256.
- [24] C. Corbella, E. Bertran, M. C. Polo, E. Pascual, J. L. Andujar, *Diam. Relat. Mater.* **2007**, *16*, 1828.
- [25] X. Chen, X. Wang, D. Fang, *Fullerenes Nanotub. Carbon Nanostructures* **2020**, *28*, 1048.
- [26] A. Morais, J. P. C. Alves, F. A. S. Lima, M. Lira-Cantu, A. F. Nogueira, *J. Photonics Energy* **2015**, *5*, 057408.
- [27] X. Ji, Y. Yang, Y. Ding, Z. Lu, G. Liu, Y. Liu, J. Song, Z. Yang, X. Liu, *J. Phys. Chem. C* **2022**, *126*, 7799.
- [28] X. Qu, Y. Liu, B. Li, B. Xing, G. Huang, H. Zhao, Z. Jiang, C. Zhang, S. W. Hong, Y. Cao, *J. Mater. Sci.* **2020**, *55*, 13062.
- [29] X. Wang, Z. Feng, X. Hou, L. Liu, M. He, X. He, J. Huang, Z. Wen, *Chem. Eng. J.* **2020**, *379*, 122371.
- [30] X. Zhu, X. Jiang, X. Liu, L. Xiao, Y. Cao, *Green Energy Environ.* **2017**, *2*, 310.
- [31] L. A. Ma, A. J. Naylor, L. Nyholm, R. Younesi, *Angew. Chemie - Int. Ed.* **2021**, *60*, 4855.
- [32] H. Kim, E. Lim, C. Jo, G. Yoon, J. Hwang, S. Jeong, J. Lee, K. Kang, *Nano Energy* **2015**, *16*, 62.
- [33] F. Zheng, Q. Deng, W. Zhong, X. Ou, Q. Pan, Y. Liu, X. Xiong, C. Yang, Y. Chen, M. Liu, *ACS Sustain. Chem. Eng.* **2018**, *6*, 16399.
- [34] Y. Zhuang, W. Zhang, Y. Bao, M. Guan, *J. Alloys Compd.* **2022**, *898*, 162848.
- [35] A. P. Nowak, P. Rutecki, M. Szkoła, K. Trzciński, *Energies* **2024**, *17*, 3233.
- [36] Y. Wei, S. Zhu, J. Bai, X. Ma, B. Zhao, X. Zhu, Z. Zi, J. Dai, *Int. J. Electrochem. Sci.* **2020**, *15*, 9081.
- [37] Z. He, Y. Huang, H. Liu, Z. Geng, Y. Li, S. Li, W. Deng, G. Zou, H. Hou, X. Ji, *Nano Energy* **2024**, *129*, 109996.
- [38] B. He, J. Cunha, Z. Hou, G. Li, H. Yin, *J. Colloid Interface Sci.* **2023**, *650*, 857.
- [39] Y. B. Rao, O. Sundman, M. Holmboe, N. Tavajohi, C. A. Ohlin, *ACS Omega* **2025**, *10*, 11158.
- [40] L. Kong, C. Zhang, J. Wang, W. Qiao, L. Ling, D. Long, *ACS Nano* **2015**, *9*, 11200.
- [41] Y. B. Rao, K. R. Achary, L. N. Patro, *ACS Omega* **2022**, *7*, 48192.
- [42] Z. Zhao, Y. Wu, R. Hu, J. Lu, D. Chen, T. Li, Y. Guo, L. Zhang, H. Chen, Z. Ye, C. Zhang, *Adv. Funct. Mater.* **2023**, *33*, 2307794.
- [43] S. Li, J. Qiu, C. Lai, M. Ling, H. Zhao, S. Zhang, *Nano Energy* **2015**, *12*, 224.
- [44] H. Li, K. Wang, W. Li, S. Cheng, K. Jiang, *J. Mater. Chem. A* **2015**, *3*, 16495.
- [45] L. Pan, H. Huang, T. Liu, M. Niederberger, *Electrochim. Acta* **2019**, *321*, 134645.
- [46] Y. Huang, X. Li, J. Luo, K. Wang, Q. Zhang, Y. Qiu, S. Sun, S. Liu, J. Han, Y. Huang, *ACS Appl. Mater. Interfaces* **2017**, *9*, 8696.
- [47] J. P. Huang, D. D. Yuan, H. Z. Zhang, Y. L. Cao, G. R. Li, H. X. Yang, X. P. Gao, *RSC Adv.* **2013**, *3*, 12593.
- [48] Y. B. Rao, C. A. Ohlin, *Sustain. Energy Fuels* **2025**, *9*, 2217.

---

Manuscript received: February 25, 2025

Revised manuscript received: June 9, 2025

Version of record online:

---